Solid Particle Erosion of a Plasma Spray – Physical Vapor Deposition Environmental Barrier Coating in a Combustion Environment

Michael J. Presby[1*] and Bryan J. Harder[1]

[1]National Aeronautics and Space Administration, Glenn Research Center Cleveland, OH 44315
* Corresponding author email: michael.presby@nasa.gov

Abstract

Environmental barrier coatings (EBCs) were developed to reduce the susceptibility of SiC-based composites to the rapid volatilization and surface recession that occurs in the presence of water vapor. Extensive research and development has been performed on EBCs, and their corresponding failure mechanisms under different environmental conditions. However, one key failure mechanism, solid particle erosion (SPE), has not been thoroughly investigated. As a result, the present work investigates the SPE behavior of a ytterbium disilicate ($Yb_2Si_2O_7$) environmental barrier coating (EBC) deposited via plasma spray-physical vapor deposition (PS-PVD). Erosion testing was performed at elevated temperature (1,200 °C) in a simulated combustion environment at the NASA Glenn Research Center Erosion Burner Rig Facility. Alumina (Al_2O_3) particles were used as the eroding media. A range of particle kinetic energies and impingement angles were investigated along with the effect of coating surface roughness. The post-erosion damage morphology was characterized using scanning electron microscopy (SEM). The SPE behavior of the PS-PVD EBC was shown to be comparable to other EBC systems reported in the literature.

Keywords: Solid particle erosion; environmental barrier coating; impact damage; elevated temperature

1. Introduction

Implementing ceramic matrix composites (CMCs) in the hot-section of gas-turbine engines can lead to increased thermal and propulsive efficiency as a result of their low density, high strength, toughness, and high temperature capability [1]. However, with respect to silicon carbide fiber-reinforced silicon carbide (SiC/SiC) CMCs (herein referred to solely as CMCs), the

SiO_2 scale responsible for oxidation resistance at high temperature is susceptible to volatilization by water vapor generated as a by-product of the combustion process. In turn, enhanced oxidation and rapid surface recession occurs resulting in a loss of structural integrity and decreased life [2-3].

To combat the volatilization and surface recession due to water vapor, environmental barrier coatings (EBCs) were developed to protect CMCs and are critical for the long life requirements of CMC components [3-4]. In order to achieve these requirements, the key EBC failure mechanisms need to be well understood. Central contributors to EBC failure are recession by water vapor, steam oxidation, thermal and thermal-mechanical fatigue, degradation by calcium-magnesium-aluminosilicate (CMAS) deposits, solid particle erosion (SPE), and foreign object damage (FOD) [3]. Many of these key contributors to EBC failure have been investigated with regard to a fundamental understanding and through the development of mitigation strategies [3-15]. However, despite its importance, there exists very little work on the SPE behavior of EBCs [16-17]. Conversely, the SPE behavior of ceramic thermal barrier coatings (TBCs) for hot section metallic materials have been characterized more extensively [18-33]. In addition, efforts to characterize and understand the SPE behavior of CMC substrate materials have also been undertaken [34-36]. As such, the purpose of this study was to investigate the SPE behavior of a ytterbium disilicate ($Yb_2Si_2O_7$) EBC deposited via plasma spray – physical vapor deposition (PS-PVD). Erosion testing was performed at elevated temperature in a simulated combustion environment using alumina (Al_2O_3) particles over a range of particle kinetic energies and impingement angles. Scanning election microscopy (SEM) was used to characterize the resultant damage morphology and understand the erosion mechanisms. A comparison of the PS-PVD EBC erosion behavior to other EBC systems reported in literature is also presented and discussed.

2. Materials and Methods

The target material system used in this work was a ytterbium disilicate ($Yb_2Si_2O_7$) EBC. The $Yb_2Si_2O_7$ coatings were deposited via PS-PVD [26, 37, 38] on 25.4-mm diameter by 3-mm thick SiC Hexoloy® SE, and 25.4 by 25.4 by 3-mm SiC Hexoloy® SA monolithic substrates. Prior to

deposition, the SiC substrates were grit blasted with cubic boron nitride (CBN) powder at 60-psi to roughen the substrate surface for adhesion [8]. The substrate surface root mean square (RMS) values after grit blasting were approximately 6 to 8-µm. The EBC was deposited directly onto the SiC substrates with no bond coat.

During deposition, the substrates were secured in place along the corners, or edge, by a nickel-chromium (NiCr) strapping that was spot welded to a 177 by 177-mm steel plate. The amount of masked area for each sample was minimized where possible. The steel plate was mounted perpendicular to the plasma at a distance of 1.0-m from the torch. The conditions for deposition are shown in Table 1. EBC thicknesses ranged from 225 – 275-µm, and the deposition time was 30 minutes.

After deposition, the EBCs were heat treated in air at 1450 °C for three hours to crystallize the coating. X-ray diffraction (XRD) was performed using a Bruker (Milwaukee, WI) D8 Diffractometer to confirm the composition and crystal structure. Representative XRD patterns are shown in Figure 1 for the as-deposited coating and after heat treatment. In the as-deposited state, there is a significant amount of amorphous phase and the crystalline content is a mixture of ytterbium disilicate, ytterbium monosilicate, and ytterbia. Upon heat treating to 1450 °C for three hours in air, the coating fully reacts and crystallizes to a composition of ytterbium disilicate with some excess SiO_2. The coating composition was determined to be approximately 77-vol% $Yb_2Si_2O_7$[a] with 23-vol% SiO_2[b]. Image analysis showed that the EBC porosity was ~5%. Based on this, the bulk density of the $Yb_2Si_2O_7$ EBC was estimated to be $\rho_{Yb2Si2O7/EBC}$ = 5.01-g/cm^3. The surface roughness values, Sa [µm], of the post heat treated EBC surfaces were measured using a Zygo 3D optical profilometer. Six locations with dimensions of 0.86 by 0.86-mm were averaged to determine the surface roughness of a given sample.

A representative cross-section of the EBC after heat treatment is displayed in Figure 2(a). Figure 2(b) shows a top-down view of the EBC surface post heat treatment where mud cracking is evident. The mud cracking that was observed post heat treatment is likely due to stresses arising as a result of a volumetric change due to crystallization and potential sintering

[a] $Yb_2Si_2O_7$, ρ = 6.15-g/cm^3 (PDF card 04-007-8967) [39]
[b] SiO_2 (low cristobalite) ρ = 2.32-g/cm^3 [40]

of the coating at temperature. Ultimately, mud cracking limits the long-term practical use of this coating, especially in terms of environmental protection as cracks allow the penetration of water vapor or other corrosive media which can accelerate material degradation. Stresses arising during thermal cycling have been shown to be a driving factor for mud cracking in EBC systems [6]. As such, information on the SPE behavior, even with the presence of mud cracking, can still be of value. Future efforts to optimize the processing parameters to prevent mud crack formation and its effect on SPE are warranted.

The erosion experiments were conducted at the NASA Glenn Research Center Erosion Burner Rig Facility [41]. The facility was developed to more accurately represent gas turbine engine erosion conditions and has historically been used to characterize the SPE behavior of TBCs [20, 22, 23], and more recently, CMCs [36]. While the development of the erosion burner rig, along with computational fluid dynamics (CFD) modeling and experimental validation have been described in detail elsewhere [20, 22, 23], an overview of the facility is described here briefly.

The facility is a modified NASA Glenn Mach 0.3 to Mach 1.0 burner rig that operates on Jet-A fuel and pre-heated air [41]. Erodent is delivered using a screw-driven powder feeder (HA 5000F-SA, Hardface Alloys, Inc.) where it is injected into the burner chamber, passes through a 19-mm exit nozzle, and accelerates downstream through a 19-mm diameter, 305-mm long unattached duct to the sample. A high temperature, spring-loaded clamshell fixture fabricated from Inconel® 601 is used to hold the sample during testing. The standoff distance between the duct exit and the center of the sample was set to 30-mm. A representative photograph and schematic of the erosion burner rig are shown in Figures 3(a) and 3(b). The burner rig can be pivoted on and off the sample for heating and cooling, and is displayed in the off, or cooling position, in Figure 3(a).

Samples were heated to 1,200 °C (2,192 °F) as measured by an Ircon Modline 7.9-µm single-color pyrometer. After reaching the target temperature, samples were exposed to alumina (Al_2O_3) particles that were fed into the burner at a rate of 2-g/min. Alumina was chosen as the erodent since it is readily available and shown to produce erosion ‘scars’ or damage similar to that observed in engine hardware [22-24]. Three different mean particle size

Al_2O_3 particles were used in this study. As determined through a particle size distribution analysis, the mean particle sizes, *d*, were: 27, 60, and 150-µm. The range of particle sizes used in this work falls within the range reported in the literature for SPE studies of thermal barrier coatings (TBCs), and other gas-turbine materials [16-36]. SEM images of the particles are shown in Figure 4.

A constant fuel/air mixture to reach the desired surface temperature was used throughout the experiment. As a result, the particle velocity, *v*, for each particle size varied. Particle velocities were measured using a high temperature double disk velocimeter [36, 42, 43]. The angle of particle impingement, α, was fixed at 90° for the 27 and 150-µm particle sizes, and was varied between 30° and 90° for the 60-µm particle size. Three samples were tested at each condition. Table 2 summarizes the erosion conditions used in this study.

Samples were subjected to multiple exposures of 30 seconds each (1-g of erodent) where the sample mass was measured before and after each successive exposure using a scale with precision of 0.01-mg. A total of 10 exposures equating to a cumulative exposure of 10-g of erodent was used for each test condition (Table 2). This amount of erodent was determined to be sufficient to reach steady-state without eroding through the EBC to the substrate. The steady-state erosion rate, *E*, at each condition was determined from a regression fit in the linear region of the cumulative mass loss versus cumulative mass erodent curve. For consistency, the regression analysis was performed on the last six data points of each curve. The erosion damage was characterized using SEM by assessing the damage morphology directly from the eroded surfaces as well as polished cross-sections.

3. Results and Discussion

3.1 *The Effect of Particle Kinetic Energy*

Representative cumulative mass loss versus cumulative mass erodent curves are shown in Figure 5 for the PS-PVD EBC at normal (90°) impingement for the three different particle sizes. For each particle size, a well-defined linear region (representing steady-state) is observed after an initial, nonlinear transient region. The transient region is represented by a higher initial rate of mass loss followed by a decrease to steady-state.

The steady-state erosion rate, *E*, determined as the slope of the linear portion of the cumulative mass loss versus cumulative mass erodent curve (Figure 5) is plotted as a function of particle kinetic energy as shown in Figure 6. Since the erosion rate is ultimately a function of the cumulative number of impact events, *E* is converted from mass loss per mass erodent [mg/g] to mass loss per particle impact [mg]. This was accomplished by multiplying *E* [mg/g] by the mass of an individual particle [g]. The mass of an individual particle was estimated using the density of Al_2O_3 (ρ_{Al2O3} = 3.95 g/cm^3), mean particle size, *d*, and approximating the particles as spheres, as commonly performed in other erosion studies in literature [43-45]. This conversion was performed since the number of particles, and hence the number of impact events, per gram of erodent will decrease as the particle size increases from 27 to 150-µm. As a result, a regression analysis between the steady-state erosion rate, *E*, and particle kinetic energy, U_k, yields the following power law formulation:

$$E = \Phi U_k^b \tag{1}$$

where Φ = 1.3 x 10^{-6} and *b* = 1.26.

Currently, there is little precedence in the literature on velocity, or kinetic energy ($U_k = ½mv^2$) dependence for SPE in EBCs. Singh et. al. [16] investigated the velocity dependence of a barium-strontium-aluminosilicate (BSAS) EBC deposited via plasma spray. Erosion testing was performed in a vacuum at a 90° impingement angle using nominal 63-µm Al_2O_3 erodent. Two particle velocities, v = 50 and 100 m/s, were used. A power law dependence with respect to velocity, $E \propto v^n$ was observed with a velocity exponent $n = 2.7$. Since only a single particle size was used, the kinetic energy dependence can be determined simply based on the relationship between kinetic energy and velocity ($E \propto U_k^b \Longrightarrow E \propto (½mv^2)^b \Longrightarrow n = 2b$). This implies a kinetic energy exponent, *b* = 1.35 for the BSAS EBC.

For other advanced ceramic coating systems, namely TBCs, Shin et. al. [28] showed that the velocity dependence for plasma spray 7 wt.% yttria-stabilized zirconia (7YSZ) at 980°C using 27-µm Al_2O_3 ranged from 1.75 ≤ n ≤ 2.27 which implies a kinetic energy dependence of 0.875 ≤ b ≤ 1.135. Similar results for other plasma sprayed TBCs were reported by Cernuschi et. al. [18]. For electron beam – physical vapor deposition (EB-PVD) TBCs, a lower velocity dependence has

been reported where $1.00 \leq n \leq 1.50$ [18, 31] which equates to a kinetic energy dependence, $0.50 \leq b \leq 0.75$.

With regard to bulk, monolithic brittle solids, theoretical formulations to model SPE have been developed based on indentation fracture mechanics where subsurface lateral cracking is assumed to be the predominate mechanism responsible for material removal [46-47]. For example, a quasi-static analysis presented by Wiederhorn and Lawn [46] which assumes that the incident particle kinetic energy is completely absorbed by the target through irreversible plasticity processes, predicts b = 22/18 (~1.22) while a modified model presented by Marshall et. al. [47] predicts b = 7/6 (~1.16). Although several experimental observations have been shown to be in accord with the theoretical predictions, the kinetic energy dependence for bulk, monolithic materials generally falls within the range $1 \leq b \leq 2$ [43-45,47-48].

In view of the preceding discussion, the kinetic energy exponent, b = 1.26 obtained for the PS-PVD EBC is in general accord with that observed for other coating systems (BSAS EBC and plasma sprayed TBCs), and falls within the dependence observed for many bulk, monolithic brittle materials.

3.2 *The Effect of Particle Impingement Angle*

The effect of impingement angle, α, on the erosion behavior was evaluated for d = 60-μm. Typical cumulative mass loss versus cumulative mass erodent curves are shown in Figure 7. Similar to normal impingement (Figure 5), a higher rate of mass loss is initially observed prior to decreasing and reaching steady-state for each angle. Figure 8 shows the steady-state erosion rate, E [mg/g], plotted as a function of α from 30° to 90°. Within this range, it is observed that E increases with increasing α, and reaches a maximum at 90°, which is a characteristic of brittle-dominated erosion behavior. A similar dependency was reported by Singh et. al. [16] and Okita et. al. [17] on other EBC systems deposited by plasma spray. This will be shown and discussed in more detail in *Section 3.5*.

3.3 *The Effect of Surface Roughness*

A transient region represented by a higher initial rate of mass loss followed by a decrease to steady-state is observed for the three different particle sizes and impingement angles reported

in this study. Based on previous related work on TBCs [26], it is believed that the initial erosion behavior is strongly influenced by the initial surface quality of the EBC. As such, the effect of the initial surface roughness on the initial erosion rate, *E'*, is evaluated for the 60-µm particle size and 30°, 60°, and 90° impingement angles. *E'* was defined as the mass loss after one gram of particle exposure, and the results are displayed in Figure 9(a). It is evident that a higher initial surface roughness corresponds to a higher initial erosion rate at each impingement angle. For comparison, Figure 9(b) shows the steady-state erosion rate, *E*, plotted as a function of the initial surface roughness where it is evident that *E* is relatively independent of the initial roughness. This suggests that surface protrusions and asperities are easily fractured and removed upon initial particle impact events leading to a higher degree of initial mass loss, similar to what has been observed and reported for TBCs [19, 26].

3.4 *Erosion Damage Morphology*

Figure 10 shows the erosion surface morphology at two different regions of the EBC for *d* = 60-µm and α = 90°. In both regions, Figure 10(a) and 10(b), plastic impressions reminiscent of an impacting particle (sharp indenter) are observed with micro-cracks, representative of a brittle mode of erosion, extending radially from the corners of the impressions.

For α = 60°, as shown in Figure 11(a) and 11(b), visible wear scars or grooves are observed as a result of the particle impacting and sliding along the surface. In Figure 11(a), displaced material is observed around an embedded particle fragment resulting from the ploughing action of the particle during impact at an oblique angle. Micro-cracking near the particle impact areas are also evident.

A further increase in grooving is observed as α is decreased to 30° as highlighted in Figure 12(a) and 12(b). This indicates that there is an increasing contribution of a plastic or ductile-like erosion process as the impingement angle decreases from 90°. Nonetheless, micro-cracking, representing a brittle failure mode, is still evident, and is observed adjacent to the grooves.

The PS-PVD EBC tested in this study has a lamellar microstructure similar to air plasma spray (APS) coatings. In APS coatings, material removal is generally associated with the delamination of single or multiple splats due to cracks propagating along splat boundaries [18, 28]. Analysis of the eroded cross-sections, displayed in Figure 13, show that similar behavior is observed in the PS-PVD EBC where near-surface cracking generally encompasses multiple splats resulting in delamination and subsequent material removal.

3.5 *Comparison of Erosion Behavior for PS-PVD EBC and Plasma Sprayed EBCs*

The erosion rate and dependencies for the PS-PVD $Yb_2Si_2O_7$ EBC in this study is compared to the work reported by Singh et. al. [16] on a plasma spray BSAS EBC, and Okita et. al. [17] on a plasma spray EBC. The composition of the EBC in Okita et. al. was not reported. Table 3 summarizes the erosion conditions used and results of those works as compared to those obtained in this study.

Okita et al. also investigated the effect of surface roughness by conducting erosion testing on as-deposited (unpolished) and polished EBC surfaces as noted in Table 3. Results showed a correlation to surface roughness where the polished samples (Ra = 0.25) had a lower erosion rate than the unpolished samples (Ra = 6.1). This is in relative agreement with the results presented in this work where the initial erosion rate increases with surface roughness. It should be noted that Okita et. al. employed a single dose of 2-g of erodent for all testing, so the reported erosion rates would also include the effect of any initial transient region.

To better elucidate a comparison between the results reported in Table 3, the erosion rate, *E,* is converted from mass loss per mass erodent [mg/g] to mass loss per particle impact [mg] as performed previously in Section 3.1. This conversion was performed to account for differences in the cumulative number of impact events arising from different particle sizes and densities. The densities ρ_{Al2O3} = 3.95-g/cm^3 for Al_2O_3, and ρ_{Quartz} = 2.65-g/cm^3 for quartz (silica) were used for the calculations.

Figure 14 shows the data in Table 3 for the normal (90°) and near-normal (80°) test conditions. Notwithstanding the assumptions used within the analysis (estimating the mass of an impacting particle), and variations in test parameters, the erosion performance among the three EBCs are similar when compared on the basis of mass loss. While a volumetric erosion

rate is preferred to account for differences in EBC composition and density, the relative density of the BSAS EBC investigated by Singh et. al., was not reported. However, considering the theoretical density of BSAS[c] is approximately 3.3-g/cm^3, and that the bulk density of the plasma sprayed EBC is likely lower when accounting for inherent porosity (i.e. $\rho_{BSAS/EBC} \leq$ 3.3-g/cm^3), it is reasonable to conclude that the PS-PVD EBC ($\rho_{Yb2Si2O7/EBC}$ = 5.01-g/cm^3) is more erosion resistant on a volumetric basis with respect to the test conditions used between the two studies. For the study performed by Okita et. al., the EBC composition and density were not reported so determining or extrapolating a relative erosion resistance on a volumetric basis between the EBC systems could not be performed.

It should also be noted for the comparison that the EBC system investigated by Okita et. al. incorporated a bond coat between the substrate and the top coat while the BSAS EBC investigated by Singh et. al., and the PS-PVD EBC in this work did not incorporate a bond coat. Since SPE damage is highly localized to the surface, the presence, or lack thereof, of a bond coat is not anticipated to play a significant role in the overall erosion rate of the EBC top coat. Nonetheless, investigations into the effect of a bond coat may be warranted; for example, understanding the influence of dynamic stress wave interactions during particle impact.

The effect of impingement angle on the erosion rate for the data reported in Table 3 is shown in Figure 15. The erosion rate is normalized with respect to the normal (90°) data for the BSAS EBC investigated by Singh et. al., and for the PS-PVD EBC from this study. For the EBC investigated by Okita et. al., the data is normalized with respect to the near-normal (80°) data. Under the assumption that the erosion rate at 80° is approximately equal to 90° [17], normalizing with respect to 80° for this case is not expected to significantly alter the observed dependence. As shown in Figure 15, a similar dependence for the erosion rate with respect to impingement angle is observed among the three EBC systems. The overall angular dependence observed by the three EBC systems is representative of brittle-dominated erosion where the maximum erosion rate occurs at 90° and decreases as the impingement angle decreases. However, as shown in this work, a plastic erosion process resulting in wear scars or grooves

[c] Hexacelsian BSAS, ρ = 3.3-g/cm^3 (PDF card – 00-026-0182) [39]
Celsian BSAS, ρ = 3.314-g/cm^3 (PDF card – 00-038-1451) [39]

contributes to material removal at lower impingement angles in the PS-PVD EBC. The comparable angular dependence suggests that a similar process may be operative in the other EBC systems as well.

4. Conclusions

SPE is a complex phenomenon that can cause detrimental effects to engine hardware. Owing to the implementation of CMCs into gas turbine engines, it is important to characterize the SPE behavior of EBCs because they are a critical technology required to protect CMCs from the harsh, water-vapor-containing combustion environment.

There are numerous factors that will affect the SPE behavior of EBCs which include EBC properties (composition, microstructure, surface condition, hardness, toughness, etc.), engine operational conditions (temperature, pressure, combustion environment, etc.), and erosion/impact conditions (particle type, particle shape, velocity/kinetic energy, impingement angle, etc.). Ultimately, the enormity of factors and their combinations requires interdisciplinary approaches in experimental characterization, modeling, and simulation to aid in the understanding of SPE and for the design and fabrication of EBCs.

In the present work, the PS-PVD $Yb_2Si_2O_7$ EBC exhibited a power law dependence of the steady-state erosion rate, *E,* with respect to particle kinetic energy of the form: $E = \Phi U_k^b$ where Φ = 1.3 x 10^{-6} and *b* = 1.26. The functional dependence with respect to kinetic energy is in general accord with other coating systems and bulk, monolithic ceramic materials reported in literature. The EBC exhibits a brittle-fracture-dominated erosion response as exemplified by the dependence on impingement angle from 30° to 90° where the EBC exhibits a maximum erosion rate at normal (90°) impingement, and decreases with lower impingement angles. SEM analysis of 90° impingement samples show plastic impressions, representative of a sharp indenter, with micro-cracking extending radially from the corners of the impression. However, SEM analysis of the eroded surfaces shows an increasing contribution of a plastic process at lower impingement angles as exemplified by wear scars, or grooves, reminiscent of the particles impacting, and sliding along the surface. Nonetheless, evidence of brittle fracture (micro-cracking) is still observed at the lower impingement angles. Cross-sections of the eroded samples show near-

surface cracking encompassing single and multiple splats leading to delamination and subsequent material removal. The surface roughness of the EBC influences the initial erosion behavior as a higher surface roughness corresponds to a higher initial erosion rate, *E'* suggesting that surface asperities and protrusions are easily fractured and removed upon impact. Finally, the PS-PVD $Yb_2Si_2O_7$ EBC erosion rate is comparable on a mass loss basis and impingement angle dependence to other EBC systems reported in the literature.

Acknowledgements

The authors gratefully acknowledge Pete Bonacuse and Wayne Jennings for their assistance with the SEM, and Doug Kiser for thoughtful discussion and comments. This work was sponsored by the NASA Aeronautics Research Mission Directorate (ARMD) Transformational Tools and Technologies Project (TTT).

References

[1] F. Zok, Ceramic-Matrix Composites Enable Revolutionary Gains in Turbine Engine Efficiency, American Ceramic Society Bulletin, 95 (5) (2016) 22-28.

[2] N. S. Jacobson, Corrosion of Silicon-based Ceramics in Combustion Environments, Journal of the American Ceramic Society, 76 (1) (1992) 3-28.

[3] K. Lee, Yb2Si2O7 Environmental Barrier Coatings with Reduced Bond Coat Oxidation Rates via Chemical Modifications for Long Life, Journal of the American Ceramic Society, 102 (3) (2019) 1507-1521.

[4] N. Padture, Environmental Degradation of High-Temperature Protective Coatings for Ceramic-Matrix Composites in Gas-Turbine Engines, Materials Degradation, 3 (11) (2019).

[5] E. Bakan, Y. J. Sohn, W. Kunz, H. Klemm, R. Vaben, Effect of Processing on High-Velocity Water Vapor Recession Behavior of Yb-Silicate Environmental Barrier Coatings, Journal of the European Ceramic Society, 39 (4) (2019) 1507-1513.

[6] B. T. Richards, S. Sehr, F. de Franqueville, M. R. Begley, H. G. Wadley, Fracture Mechanisms of Ytterbium Monosilicate Environmental Barrier Coatings during Cyclic Thermal Exposure, Acta Materialia, 103 (2016) 448-460.

[7] M. P. Appleby, D. Zhu, G. N. Morscher, Mechanical Properties and Real-Time Damage Evaluations of Environmental Barrier Coated SiC/SiC CMCs Subjected to Tensile Loading under Thermal Gradients, Surface and Coatings Technology, 284 (2015) 318-326.

[8] B. J. Harder, M. J. Presby, J. A. Salem, S. M. Arnold, S. K. Mital, Environmental Barrier Coating Oxidation and Adhesion Strength, Journal of Engineering for Gas Turbines and Power, 143 (3) (2021) 031004-031004-6.

[9] K. M. Grant, S. Kramer, J. Lofvander, C. G. Levi, CMAS Degradation of Environmental Barrier Coatings, Surface and Coatings Technology, 202 (4-7) (2007) 653-657.

[10] D. L. Poerschke, J. S. Van Sluytman, K. B. Wong, C. G. Levi, Thermochemical Compatibility of Ytterbia (Hafnia/Silica) Multilayers for Environmental Barrier Coatings, Acta Materialia, 61, (18) (2013) 6743-6755.

[11] V. L. Wiesner, B. J. Harder, N. P. Bansal, High-Temperature Interactions of Desert Sand CMAS Glass with Yttrium Disilicate Environmental Barrier Coating Material, Ceramics International, 44 (18) (2018) 22738-22743.

[12] V. L. Wiesner, D. Scales, N. S. Johnson, B. J. Harder, A. Garg, N. P. Bansal, Calcium-Magnesium Aluminosilicate (CMAS) Interactions with Ytterbium Silicate Environmental Barrier Coating Materials at Elevated Temperatures, Ceramic International, 46 (10) (2020) 16733-16742.

[13] R. T. Bhatt, S. R. Choi, L. M. Cosgriff, D. S. Fox, K. N. Lee, Impact Resistance of Environmental Barrier Coated SiC/SiC Composites, Materials Science and Engineering A, 476 (1-2) (2008) 8-19.

[14] N. Kedir, E. Garcia, C. Kirk, J. Gao, Z. Guo, X. Zhai, T. Sun, K. Fezzaa, S. Sampath, W. W. Chen, Impact Damage of Narrow Silicon Carbide (SiC) Ceramics with and without Environmental Barrier Coatings (EBCs) by Various Foreign Object Debris (FOD) Simulants, Surface and Coatings Technology, 407 (2021).

[15] N. Kedir, E. Garcia, C. Kirk, Z. Guo, J. Gao, X. Zhai, T. Sun, K. Fezzaa, S. Sampath, W. Chen, In Situ Characterization of Foreign Object Damage (FOD) in Environmental-Barrier-Coated Silicon Carbide (SiC) Ceramic, Journal of the American Ceramic Society, 103 (8) (2020) 4586-4601.

[16] S. Singh, D. Singh, J. P. Singh, R. N. Singh, J. L. Routbort, Solid Particle Erosion of Thin Films Deposited on Ceramics, Advances in Ceramic Coatings and Ceramic-Metal Systems: Ceramic Engineering and Science Proceedings, 26, pp. 190-198, 2005.

[17] Y. Okita, Y. Mizokami, J. Hasegawa, Experimental and Numerical Investigation of Environmental Barrier Coated Ceramic Matrix Composite Turbine Airfoil Erosion, Journal of Engineering for Gas Turbines and Power, 141 (3) (2019) 031013-031013-10.

[18] F. Cernuschi, L. Lorenzoni, S. Capelli, C. Guardamagna, M. Krager, R. Vaben, K. von Niessen, N. Markocsan, J. Menuey, C. Giolli, Solid Particle Erosion of Thermal Spray and Physical Vapour Deposition Thermal Barrier Coatings, Wear, 271 (2011) 2909-2918.

[19] A. G. Davis, D. H. Boone, A. V. Levy, Erosion of Ceramic Thermal Barrier Coatings, Wear, 110 (1986) 101-116.

[20] M. A. Kuczmarski, R. A. Miller, D. Zhu, CFD-Guided Development of Test Rigs for Studying Erosion and Large-Particle Damage of Thermal Barrier Coatings, Modelling and Simulation in Engineering, (2011).

[21] S. Mahade, N. Curry, S. Bjorklund, N. Markocsan, P. Nylen, R. Vaben, Erosion Performance of Gadolinium Zirconate-Based Thermal Barrier Coatings Processed by Suspension Plasma Spray, Journal of Thermal Spray Technology, 26 (2017) 108-115.

[22] R. A. Miller, M. A. Kuczmarski, Burner Rig for Small Particle Erosion Testing of Thermal Barrier Coatings, Journal of Testing and Evaluation, 42 (3) (2014) 1-11.

[23] R. A. Miller, M. A. Kuczmarski, D. Zhu, Burner Rig with an Unattached Duct for Evaluating the Erosion Resistance of Thermal Barrier Coatings, NASA/TM – 20110013364 (2011).

[24] R.W. Bruce, Development of 1232 °C (2250 °F) Erosion and Impact Tests for Thermal Barrier Coatings, Tribology Transactions, 41 (4) (1998) 399-410.

[25] J. R. Nicholls, M. J. Deakin, D. S. Rickerby, A Comparison Between the Erosion Behaviour of Thermal Spray and Electron Beam Physical Vapour Deposition Thermal Barrier Coatings, Wear, 223-235 (1999) 352-361.

[26] M. P. Schmitt, B. J. Harder, D. E. Wolfe, Process-Structure-Property Relations for the Erosion Durability of Plasma Spray-Physical Vapor Deposition (PS-PVD) Thermal Barrier Coatings, Surface and Coatings Technology, 197 (2016) 11-18.

[27] L. Steinberg, R. Naraparaju, M. Heckert, C. Mikulla, U. Schulz, C. Leyens, Erosion Behavior of EB-PVD 7YSZ Coatings under Corrosion/Erosion Regime: Effect of TBC Microstructure and the CMAS Chemistry, Journal of the European Ceramic Society, 38 (2018) 5101-5112.

[28] D. Shin, A. Hamed, Influence of Micro-Structure on Erosion Resistance of Plasma Sprayed 7YSZ Thermal Barrier Coating under Gas Turbine Operating Conditions, Wear, 396-397 (2018) 34-47.

[29] R. Swar, A. Hamed, D. Shin, N. Woggon, R. Miller, Deterioration of Thermal Barrier Coated Turbine Blades by Erosion, International Journal of Rotating Machinery (2012).

[30] R. G. Wellman, J. R. Nicholls, A Review of the Erosion of Thermal Barrier Coatings, Journal of Physics D: Applied Physics, 40 (16) (2007) 293-305.

[31] R. G. Wellman, J. R. Nicholls, A Monte Carlo Model for Predicting the Erosion Rate of EB PVD TBCs, Wear, 256 (2004) 889-899.

[32] R. G. Wellman, J. R. Nicholls, On the Effect of Ageing on the Erosion of EB-PVD TBCs, Surface and Coatings Technology, 177-178 (2004) 80-88.

[33] R. Wellman, G. Whitman, J. R. Nicholls, CMAS Corrosion of EB PVD TBCs: Identifying the Minimum Level to Initiate Damage, International Journal of Refractory Metals & Hard Materials, 28 (2010) 124-132.

[34] N. Kedir, C. Gong, L. Sanchez, M. J. Presby, S. Kane, D. C. Faucett, S. R. Choi, Erosion in Gas-Turbine Grade Ceramic Matrix Composites, Journal of Engineering for Gas Turbines and Power, 141 (1) (2019) 011019-011019-9.

[35] M. J. Presby, C. Gong, S. Kane, N. Kedir, A. Stanley, D. C. Faucett, S. R. Choi, Erosion in a Melt-Infiltrated SiC/SiC Ceramic Matrix Composite, Journal of Engineering for Gas Turbines and Power, 142 (4) (2020) 041009-041009-9.

[36] M. J. Presby, Influence of Particle Velocity and Impingement Angle on Elevated Temperature Solid Particle Erosion of SiC/SiC Ceramic Matrix Composites, NASA/TM-20205003560, (2020).

[37] B. J. Harder, D. Zhu, M. P. Schmitt, D. E. Wolfe, Microstructural Effects and Properties of Non-line-of-Sight Coating Processing via Plasma Spray-Physical Vapor Deposition, Journal of Thermal Spray Technology, 26 (2017) 1052-1061.

[38] B. J. Harder, Oxidation Performance of Si-HfO2 Environmental Barrier Coating Bond Coats Deposited via Plasma Spray-Physical Vapor Deposition, Surface and Coatings Technology, 384 (2020).

[39] S. Gates-Rector, T. Blanton, The Powder Diffraction File: A Quality Materials Characterization Database, Powder Diffraction, 34 (4) (2019) 352–360.

[40] W. Pabst, E. Gregorova, Elastic Properties of Silica Polymorphs – A Review, Ceramics – Silikaty, 57 (3) (2013) 167-184.

[41] D. S. Fox, R. A. Miller, D. Zhu, M. Perez, M. D. Cuy, R. C. Robinson, Mach 0.3 Burner Rig Facility at the NASA Glenn Materials Research Laboratory, NASA/TM-2011216986 (2011).

[42] A. W. Ruff, L. K. Ives, Measurement of Solid Particle Velocity in Erosive Wear, Wear, 35 (1975) 195-199.

[43] S. M. Wiederhorn, B. J. Hockey, Effect of Material Parameters on the Erosion Resistance of Brittle Materials, Journal of Materials Science, 18 (1983) 766-780.

[44] J. E. Ritter, P. Strzepa, K. Jakus, L. Rosenfeld, K. J. Buckman, Erosion Damage in Glass and Alumina, Journal of the American Ceramic Society, 67 (11) (1984) 769-774.

[45] J. E. Ritter, Erosion Damage in Structural Ceramics, Materials Science and Engineering, 71 (1985) 195-201.

[46] S. M. Wiederhorn, B. R. Lawn, Strength Degradation of Glass Impacted with Sharp Particles: I, Annealed Surfaces, Journal of the American Ceramic Society, 62 (1-2) (1979) 66-70.

[47] D. B. Marshall, B. R. Lawn, A. G. Evans, Elastic/Plastic Indentation Damage in Ceramics: The Lateral Crack System, Journal of the American Ceramic Society, 65, (11) (1982) 561-566.

[48] R. O. Scattergood, J. L. Routbort, Velocity and Size Dependences of the Erosion Rate in Silicon, Wear, 67 (1981) 227-232.

Figures

Fig. 1. Representative XRD patterns of the as-deposited $Yb_2Si_2O_7$ EBC, and after heat treatment in air at 1450 °C for three hours.

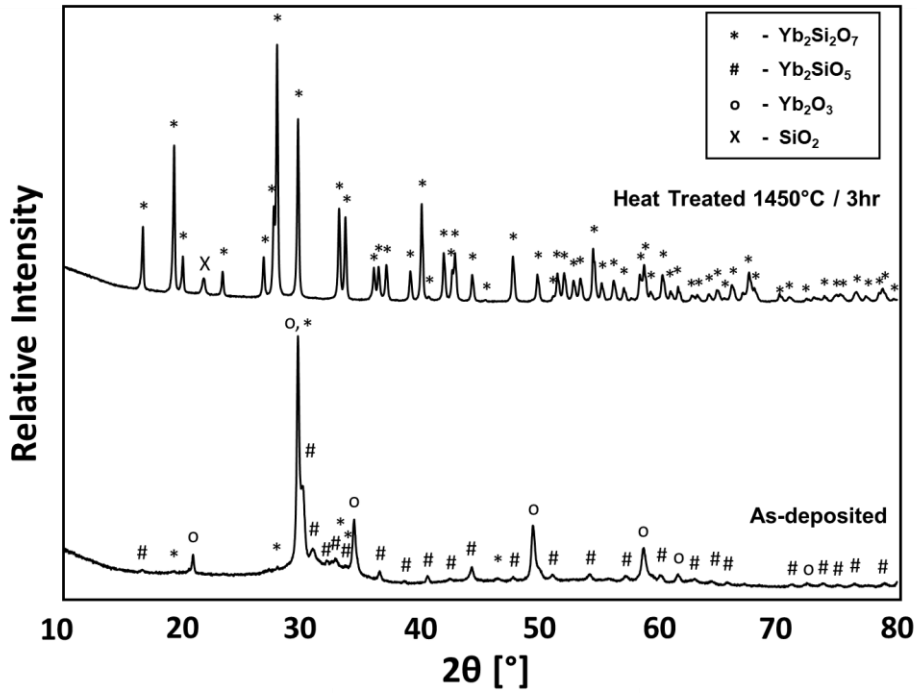

Fig. 2. Post heat treatment SEM images of the PS-PVD $Yb_2Si_2O_7$ EBC: (a) Cross-section. (b) Top-down view of the EBC surface showing mud crack.

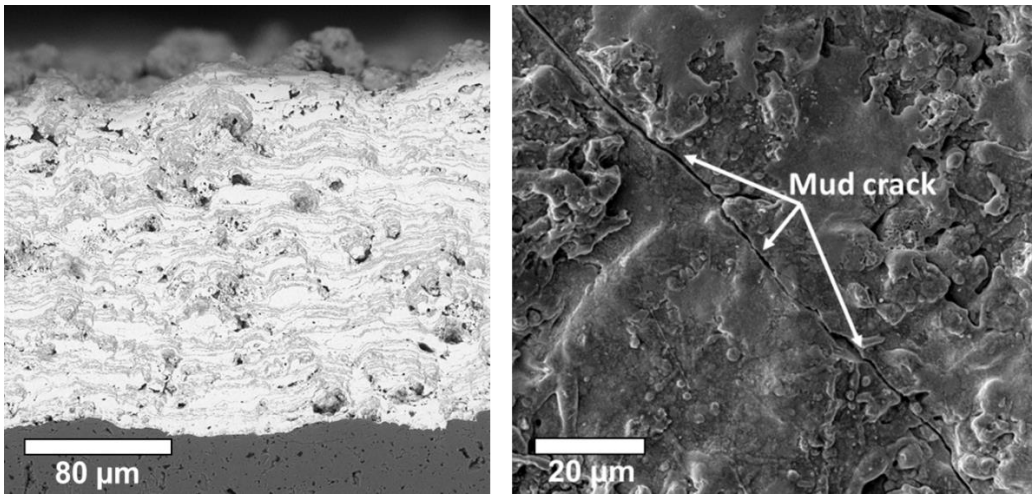

(a) (b)

Fig. 3. Erosion burner rig configuration: (a) Burner exit nozzle, 305-mm unattached duct, pyrometer and clamshell sample fixture. (b) Schematic of the burner placed before the duct [36, 41].

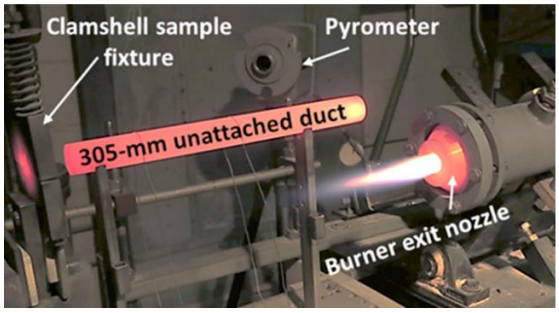

(a)

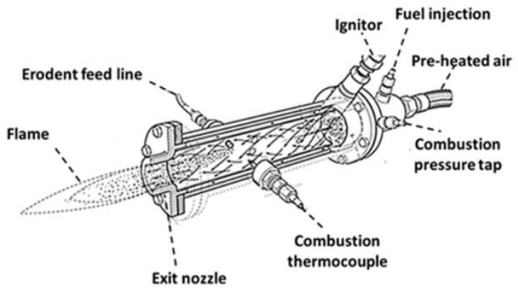

(b)

Fig. 4. SEM images of the Al_2O_3 particles used in this study: (a) 27-µm. (b) 60-µm. (c) 150-µm.

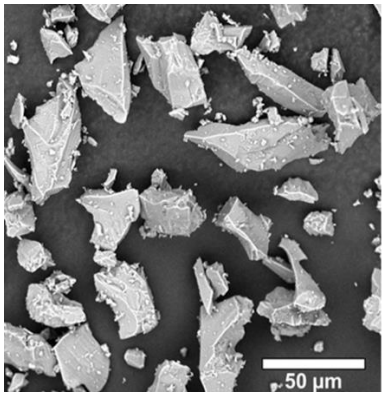

(a)

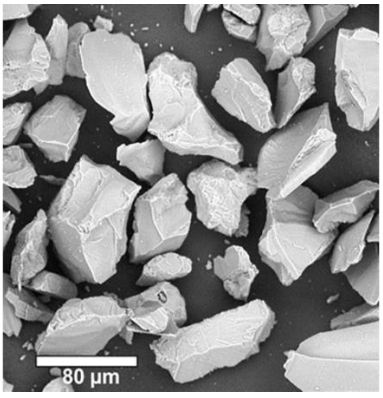

(b)

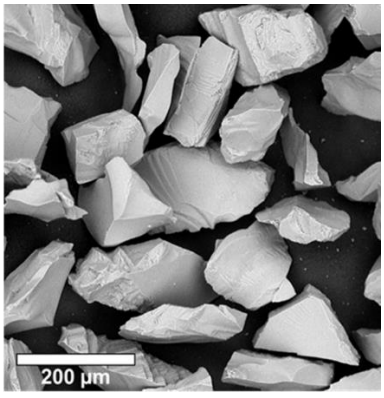

(c)

Fig. 5. Cumulative mass loss versus cumulative mass erodent for particle sizes, *d* = 27, 60, and 150-µm, and impingement angle, α = 90°.

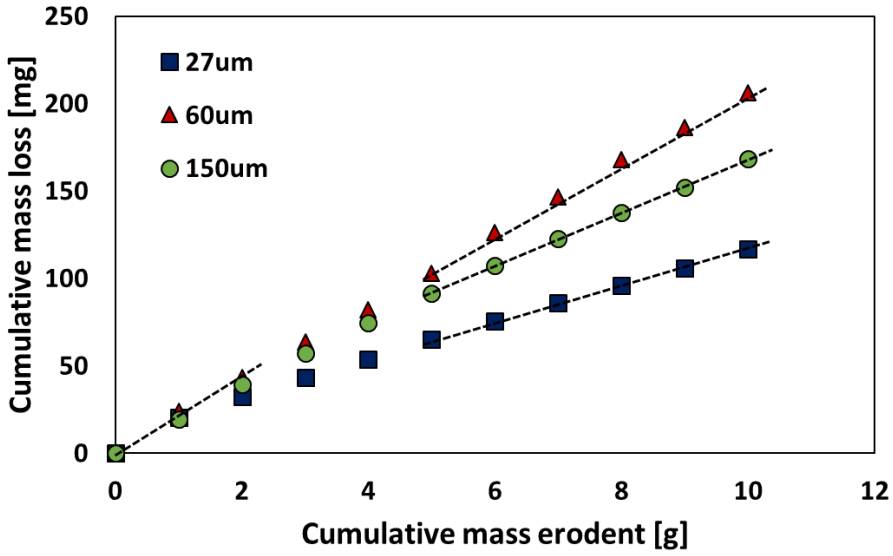

Fig. 6. Steady-state erosion rate, *E* [mg/impact] plotted as a function of particle kinetic energy, U_k [µJ], and impingement angle, α = 90°.

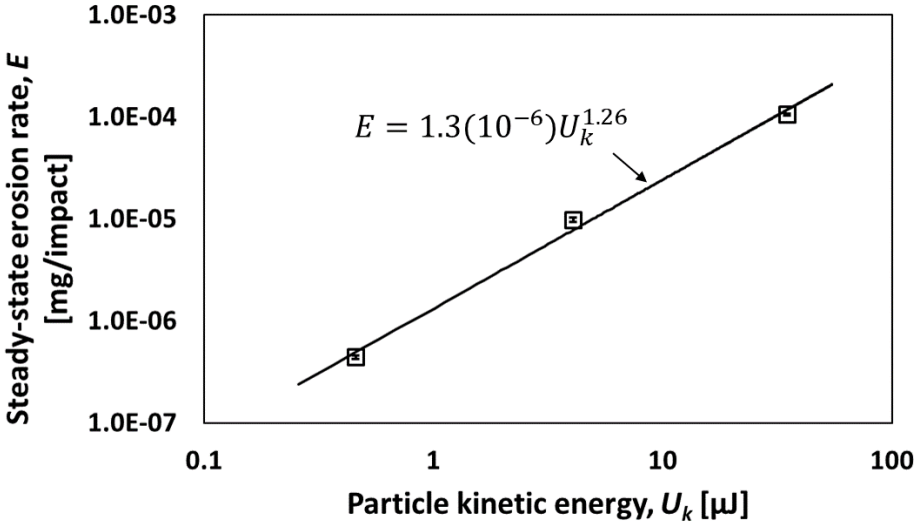

Fig. 7. Cumulative mass loss versus cumulative mass erodent for particle size, *d* = 60-µm and impingement angles, *α* = 30°, 60°, and 90°.

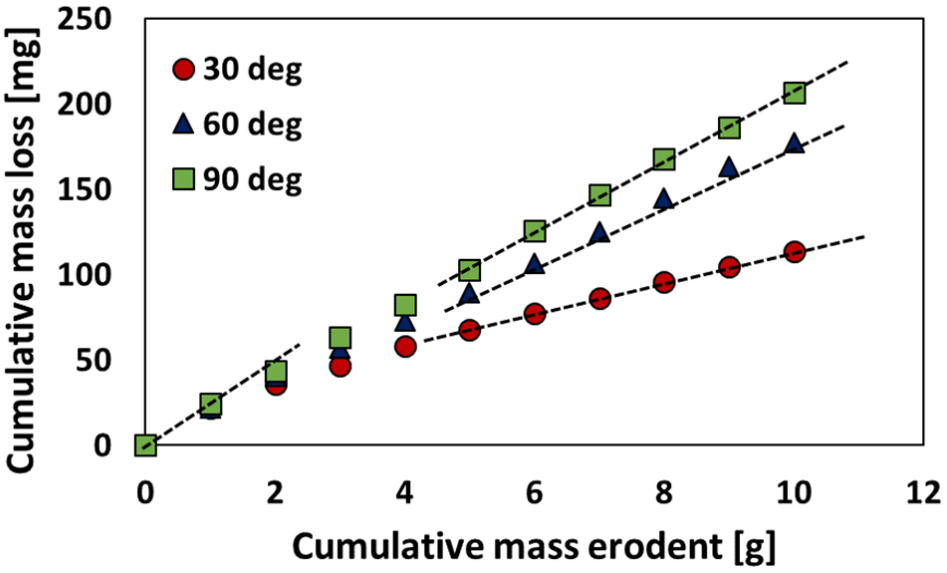

Fig. 8. Steady-state erosion rate, *E* [mg/g] plotted as a function of impingement angle, *α* [°] for particle size, *d* = 60-µm.

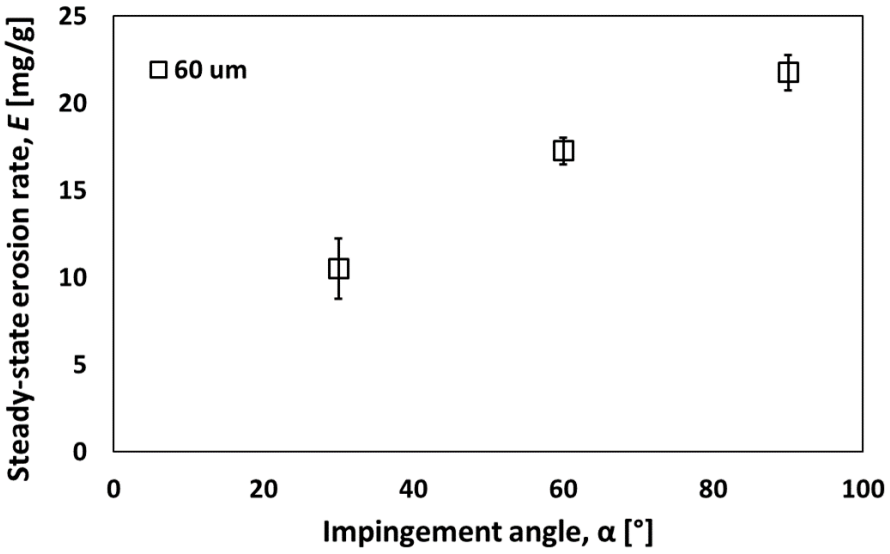

Fig. 9. The effect of surface roughness: (a) Initial erosion rate, *E'* [mg/g] (defined as the mass loss after 1-g of particle exposure) plotted as a function of initial surface roughness [µm]. (b) Steady-state erosion rate, *E* [mg/g] plotted as a function of initial surface roughness [µm].

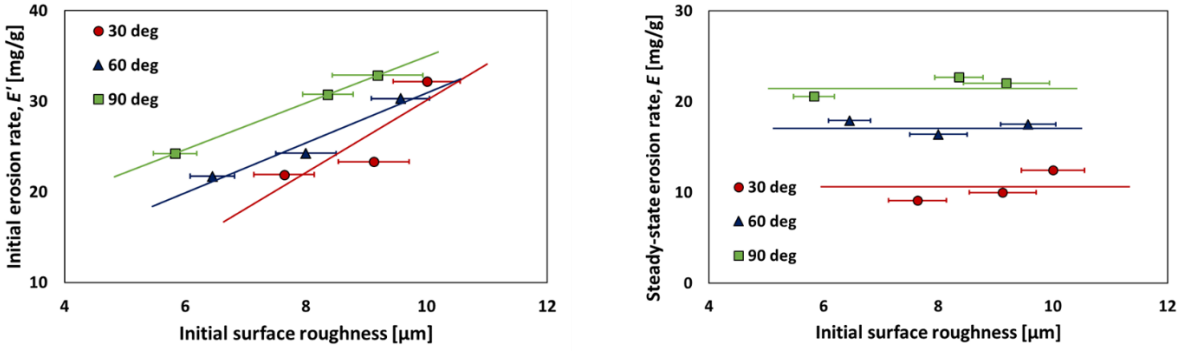

(a) (b)

Fig. 10. Erosion surface morphologies for particle size, *d* = 60-µm, particle velocity, *v* = 135 m/s, and impingement angle, *α* = 90°: (a) Region 1. (b) Region 2.

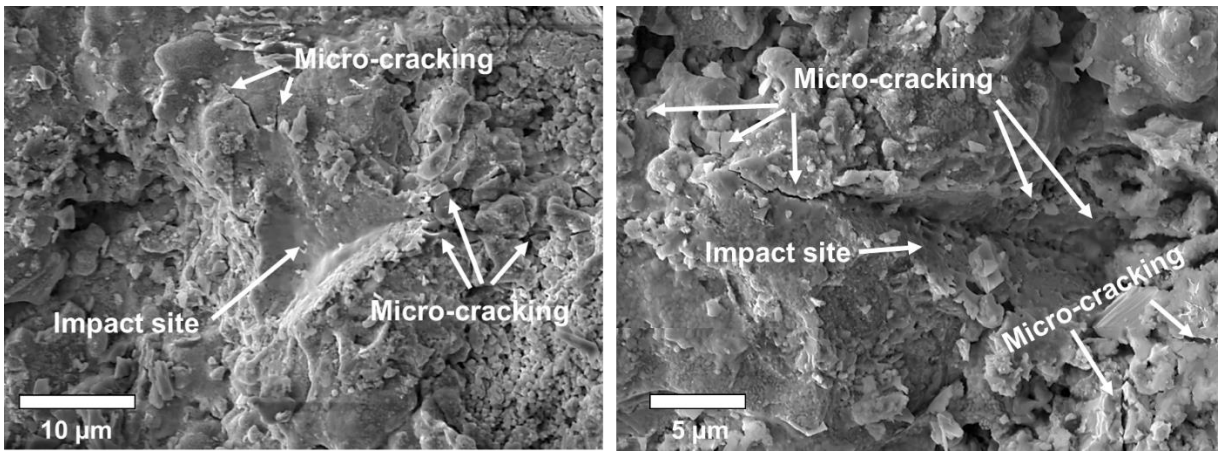

(a) (b)

Fig. 11. Erosion surface morphologies for particle size, *d* = 60-µm, particle velocity, *v* = 135 m/s, and impingement angle, *α* = 60°: (a) Region 1. (b) Region 2.

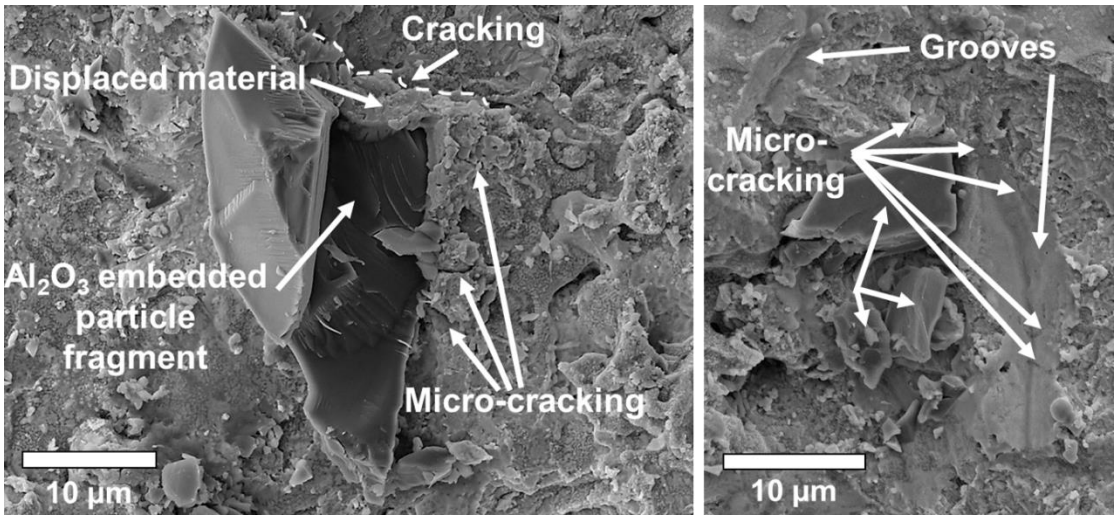

(a) (b)

Fig. 12. Erosion surface morphologies for particle size, *d* = 60-µm, particle velocity, *v* = 135 m/s, and impingement angle, *α* = 30°: (a) Region 1. (b) Region 2.

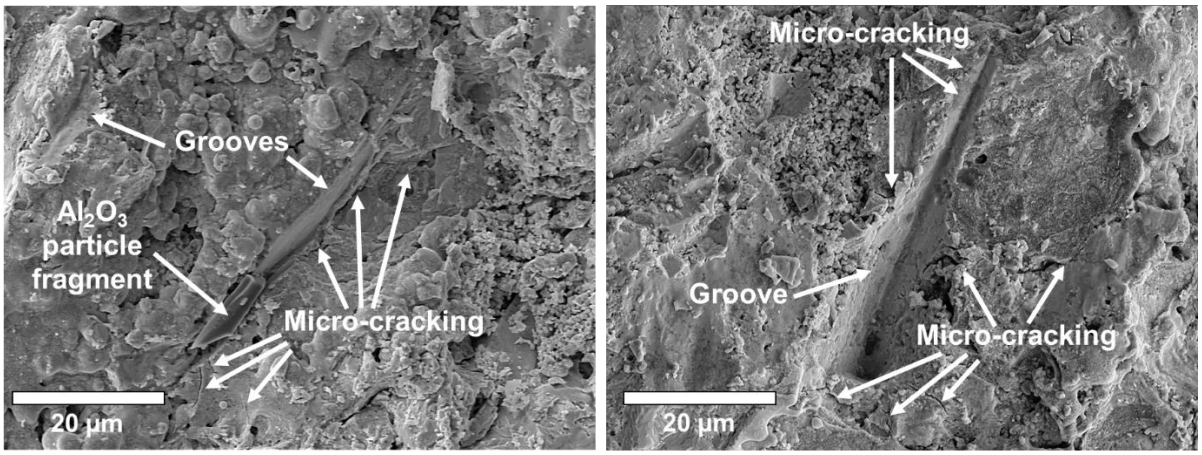

(a) (b)

Fig. 13. Cross-section damage morphology showing sub-surface damage at impingement angle, α = 90° for: (a) particle size, d = 27-µm, and particle velocity, v = 150 m/s. (b) particle size, d = 60-µm, and particle velocity, v = 135 m/s. (c) particle size, d = 150-µm, and particle velocity, v = 100 m/s. Sub-surface cracking highlighted for clarity.

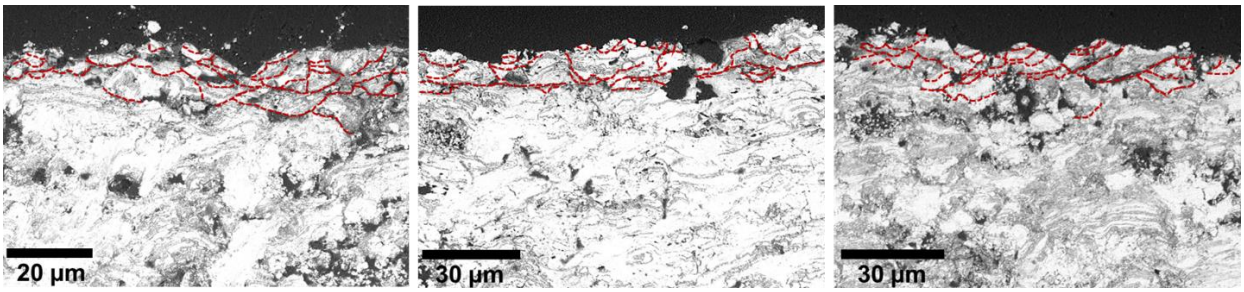

(a) (b) (c)

Fig. 14. Comparison of the erosion rate, E [mg/impact] plotted as a function of particle kinetic energy, U_k [µJ] for the normal (90°) and near-normal (80°) for the data presented in Table 3.

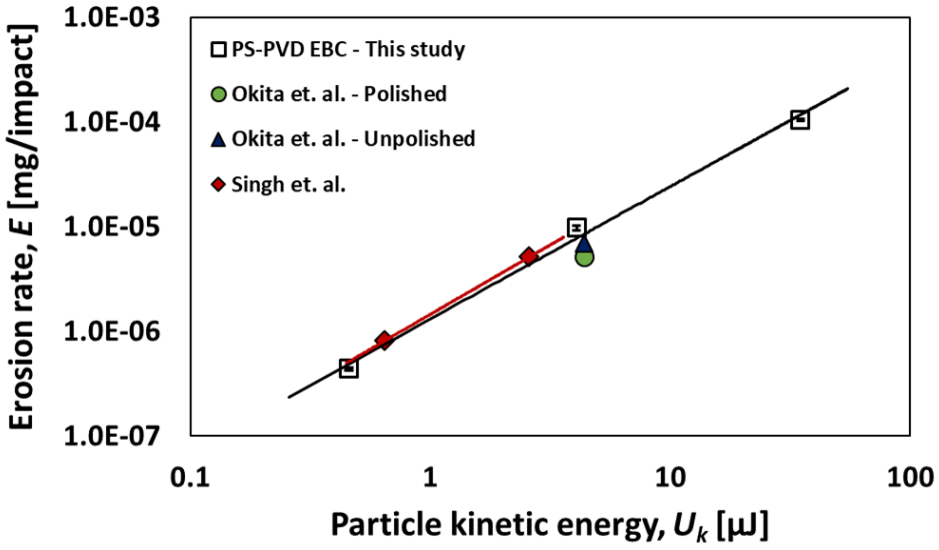

Fig. 15. Comparison of the normalized erosion rate, *E** plotted as a function of impingement angle, *α* [°] for the data presented in Table 3.

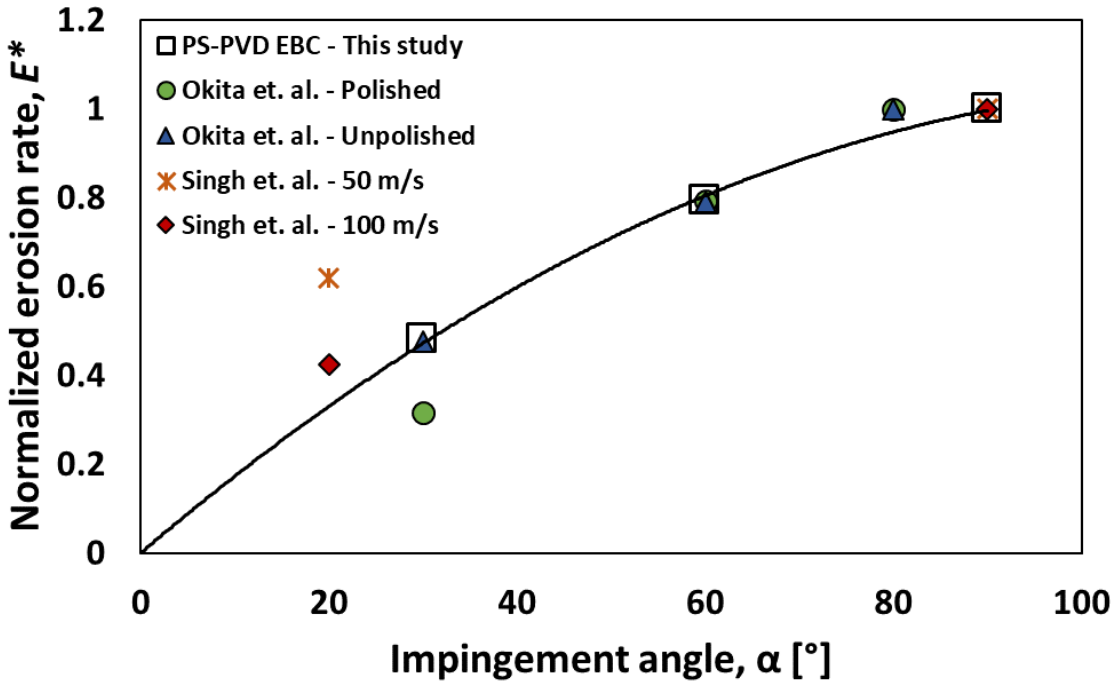

Tables

Table 1. PS-PVD processing parameters for the $Yb_2Si_2O_7$ EBC evaluated in this study.

PS-PVD Processing Parameters	
Current [A]	1640
Argon/Helium Ratio [NLPM]	30/60
Standoff Distance [m]	1.0
Pressure [torr]	0.83
EBC Target Thickness [μm]	225-275

Table 2. Erosion test conditions used in this study.

Mean Particle Size, *d* [µm]	Impingement angle, α [°]	Velocity, *v* [m/s]	Kinetic Energy[1], U_k [µJ]
27	90	150	0.46
60	30, 60, 90	135	4.07
150	90	100	34.90

[1] Kinetic energy, $U_k = ½mv^2$, was calculated by using the velocity, *v* [m/s], and the mass of an individual particle [kg]. The mass of an individual particle was estimated by using the density of Al_2O_3 (ρ_{Al2O3} = 3.95 g/cm^3), mean particle size, *d*, and approximating the particles as spheres.

Table 3. Comparison of the erosion rate, *E* for the PS-PVD $Yb_2Si_2O_7$ EBC (this study), and other EBCs reported in the literature.

Reference	Temperature [°C]	Particle Type	Particle Size, *d* [μm]	Impingement Angle, α [°]	Velocity, *v* [m/s]	Erosion Rate, *E* [mg/g]
Singh et. al. [16] (BSAS)	- (vacuum)	Al_2O_3	63	90	50	1.57
					100	9.88
				20	50	0.97
					100	4.19
Okita et. al. [17]	1037	Quartz (Silica)	50	80	225	29.57[1] (39.97[2])
				60		23.45[1] (31.61[2])
				30		9.32[1] (19.05[2])
This study ($Yb_2Si_2O_7$)	1200	Al_2O_3	27	90	150	10.72[3]
			60	90	135	21.75[3]
				60		17.25[3]
				30		10.51[3]
			150	90	100	14.95[3]

[1]Polished EBC surface erosion rate, *E*; Ra = 0.25 [17]
[2]Unpolished EBC surface erosion rate, *E*; Ra = 6.1 [17]
[3]Steady-state erosion rate, *E* (average of three samples)